

Article

Digital Twin-Based Numerical Simulation Method for Cee-Shape Cold-Formed Steel Members

Pengfei Du ¹, Xi Zhao ^{1,*}, Zhidong Zhang ² , Xiaoyan Sun ¹ and Gang Du ³

¹ School of Civil and Transportation Engineering, Beijing University of Civil Engineering and Architecture, Beijing 100044, China

² Sonny Astani Department of Civil and Environmental Engineering, University of Southern California, Los Angeles, CA 90089, USA

³ Beijing Intelligent Prefabricated Building Research Institute, Beijing 100000, China

* Correspondence: zhaoxi@bucea.edu.cn; Tel.: +86-189-0235-8188

Abstract: Cold-formed steel (CFS) structures are widely used in construction and infrastructure due to their lightweight and high-strength properties. However, their thin-walled nature makes them geometrically sensitive to compressive loading. The Digital Twin (DT)-based numerical simulation method is developed using the actual geometries of CFS shapes, which are acquired by a 3D laser scanner. The DT-based numerical simulation incorporates the reconstructed measurement point clouds into the finite element modeling, ensuring that actual geometric features are retained. A series of tests, including material and axial compression testing, are conducted to validate the modeling parameters, such as mesh sizes and boundary conditions. The advantages of the DT-based numerical simulation method are highlighted compared to the traditional CFS member numerical simulation, which incorporates only the first mode of geometric imperfection. Additionally, DT-based numerical simulations offer more accurate load capacities and deformation predictions. Moreover, the automated and validated DT-based numerical simulation demonstrates prevalence in modeling efficiency and computation effectiveness. The DT-based numerical simulation method holds potential for application in smart structural analysis, where accurate geometries derived from extensive measurement point clouds are integrated into numerical modeling.

Keywords: digital twin-based numerical simulation; cold-formed steel; 3D laser scanner; testing validation



Citation: Du, P.; Zhao, X.; Zhang, Z.; Sun, X.; Du, G. Digital Twin-Based Numerical Simulation Method for Cee-Shape Cold-Formed Steel Members. *Buildings* **2023**, *13*, 2388. <https://doi.org/10.3390/buildings13092388>

Academic Editor: Hassan Karampour

Received: 17 August 2023

Revised: 7 September 2023

Accepted: 13 September 2023

Published: 20 September 2023



Copyright: © 2023 by the authors. Licensee MDPI, Basel, Switzerland. This article is an open access article distributed under the terms and conditions of the Creative Commons Attribution (CC BY) license (<https://creativecommons.org/licenses/by/4.0/>).

1. Introduction

Cold-formed steel (CFS) members are manufactured at room temperature, offering benefits such as high strength, ease of transportation, and rapid erection and construction. However, the thin-walled characteristic of CFS members makes them sensitive to strength variations based on their geometries [1]. Although manufacturing tolerances are well controlled, transportation and storage can introduce additional geometric imperfections to the CFS members [2,3]. Consequently, predicting structural performance becomes more challenging due to random geometry deviations during numerical simulations. Traditional numerical simulations typically introduce an initial imperfection to the CFS models, with shapes based on the first buckling modes [4]. The magnitude of the imperfection is determined as $L/960$ by both Chinese [5] and North American standards [4]. However, modern structural design trends lean towards analysis-based or simulation-based approaches, wherein nonlinear structural performance is a crucial consideration [6,7]. Traditional numerical simulations fall short of meeting the demands of structural analysis, particularly for CFS members [8]. Accurate simulations for strength predictions must consider the real-world conditions of CFS members, such as their true geometry.

Measurement techniques are crucial for obtaining geometric information about CFS members. Over the past decades, measurements have evolved from contact-based to non-

contact approaches [9,10]. Traditional contact measurements employ displacement sensors, calipers, and rulers to gauge geometric surface textures, cross-section dimensions, and specimen length. Consequently, the geometric imperfections incorporated into numerical simulations might not adequately represent the actual impacts of geometry on the strength of CFS members. On the other hand, non-contact measurements of CFS members predominantly utilize optical measurement techniques, such as laser-scanning triangulation (Figure 1) [10,11] and photography DIC techniques [12]. Such member-level measurements are more common in laboratories than in the industry. Limitations of these techniques include cost and efficiency. DIC techniques necessitate multiple high-resolution cameras and specialized software for measurements. Both research costs and device expenses can be prohibitive. Furthermore, the precision of these measurements might exceed the necessary qualifications [13]. Laser-based measurement seems more pragmatic, but challenges arise in reconstructing measurements and their application in structural analysis.

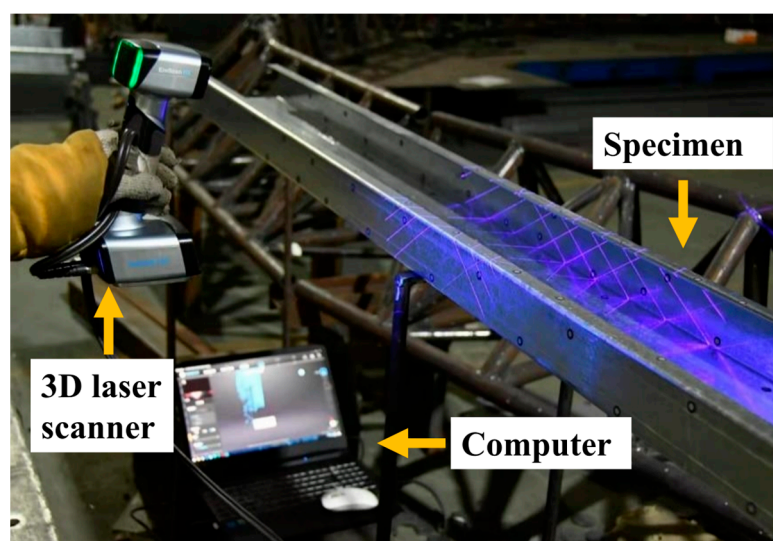


Figure 1. Laser-scanning triangulation technique.

Reconstruction of laser measurements has advanced in recent years. While commercial software is not yet tailored for structural member applications, fundamental surface registration from scanned segments is achievable. Users can register scanned segments of items from various angles using geometric features or calibration markers [14,15]. Additionally, such software can only compute the area and dimensions of regions specified by users. The level of automation in image processing for measurements is not satisfactory, especially considering the unstructured data in structural applications. As a solution, Zhao et al. [11] proposed a post-processing algorithm that can automatically filter measurement noises and reorganize data for Zee-shaped section members. The post-processing algorithm processes data section by section. Section positions were determined through hardware records. A maximal curvature test was conducted on segments sequentially within a cross-section, identifying four maximum curvatures. These maximal curvatures were deemed the corners of the cross-section, while other segments represented flat regions such as webs, flanges, and lips. This method organized the data structure of the Zee-shaped sections for simpler structural and dimensional analysis. However, this approach was solely applied to Zee-shaped sections measured on a laboratory laser platform.

Feng et al. [10] and Xu [16] also introduced a post-processing method for measurements from a hand-held laser scanner, specifically RASNAC and geometric model reconstruction. Given that the targets are thick, hot-rolled steel sections, the resolution requirements for measurements are not as stringent as those for CFS members. Cross-sectional features are defined using several straight lines, enabling the intelligent identification of flanges and webs. Zhao [8] later proposed a new robust feature recognition method that

fits other shapes of CFS members. The new robust feature recognition method is suitable for various shapes of CFS members. This method is globally optimized, ensuring more accurate feature recognition. The data structure is organized based on the geometric features of structural members, such as webs, flanges, lips, and corners. This geometric feature data structure can be utilized for various applications in the field, including identifying geometric imperfections [10,11,17] or detecting deformations [16]. The reorganized reconstructed models can be viewed as digital twins, where the organized point clouds accurately represent the genuine geometric conditions of the measured structural members [18,19].

The cutting-edge technology, digital twin, is being explored for broader applications in structural research fields, such as numerical simulations of structural members [20]. The geometric properties of steel members play a pivotal role in structural analysis and can be accurately characterized using laser measurements [21]. Meanwhile, researchers have identified imperfections in measured CFS members [22,23], the magnitudes of which were statistically analyzed and incorporated into numerical simulations. Nevertheless, there is potential for further development in this application. Specifically, the geometry of digital twins could be directly integrated into finite element modeling [11,24]. However, the practical application of this research has been limited due to the computational demands of processing large point clouds and the potential for divergence in numerical simulation. Moreover, these DT-based finite element models have yet to undergo validation through testing.

This research focuses on developing a DT-based numerical simulation method for CFS members to achieve enhanced computational speeds in finite element models. These models are calibrated using axial compression tests on 27 Cee-shaped CFS members. The subsequent section introduces the research background. In Section 3, we detail the DT-based numerical simulation methods. Section 4 provides testing methodologies, leading to model validation discussions in Section 5. Section 6 contrasts the DT-based numerical simulations against traditional approaches. Additionally, this section delves into the implications of varying simulation parameters. Conclusions and prospects for future research are encapsulated in Section 7.

2. Background

This research is based on point-cloud models of cold-formed steel members measured using a hand-held laser scanner. Digital twins of the CFS members are constructed using the feature recognition algorithm outlined in [11]. Twenty-seven CFS member tests are included for validation and comparative analysis.

2.1. Laser Measurements

An EinScan HX laser scanner is utilized in the research, as shown in Figure 2a. The EinScan HX scanner features a camera and a detector, utilizing triangulation measurement technology for swift positioning and data capture. The scanner gathers optical data and transmits it to a computer via transmission wires. Accompanying the laser scanner is the EXScan HX software, used for real-time reconstruction of the measurements. The recommended scanning distance ranges between 370 mm and 570 mm, with a measurement accuracy reaching up to 0.04 mm.

The scanning process begins with the placement of markers on the target specimens. These markers are arranged according to the triangulation measurement principle, forming triangles with edge distances ranging from 100 mm to 150 mm, as illustrated in Figure 2b. Given the regular geometric shapes of the CFS specimens, the laser scanning mode is selected. Before scanning, procedures are set for brightness adjustment, surface detection, and texture sourcing. The scan proceeds, with real-time measurement pieces visualized via the EXScan HX software. Subsequent pre-processing steps are performed within the software, such as denoising and segmenting the point clouds. An example of the scanned point clouds can be viewed in Figure 3.

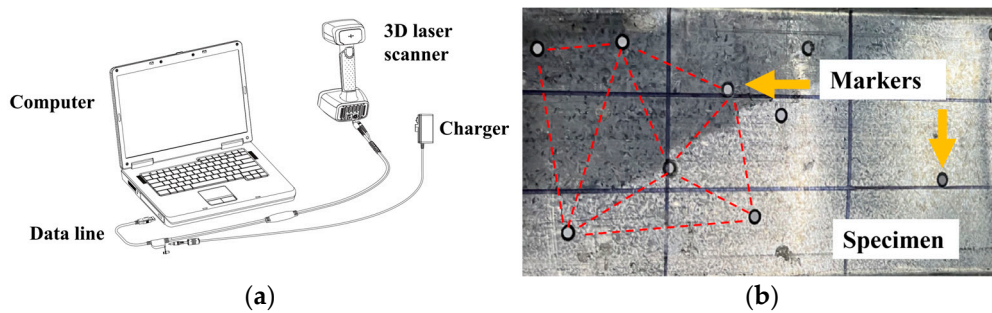


Figure 2. Laser scanner and scanning specimen: (a) EinScan HX laser scanner; (b) Markers' arrangement by triangulation.

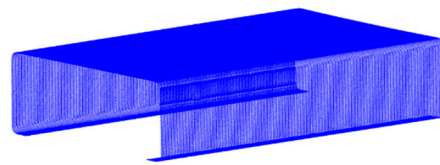


Figure 3. Scanning result of the CFS Cee specimen.

2.2. Post-Processing

The pre-processed point clouds of CFS members are unsuitable for direct application in structural analysis. The data structures of these reconstructed point cloud data (PCd) models are imperfect, characterized by disordered points and undefined geometric features. As a result, direct identification of dimensions and surface textures becomes challenging. This necessitates the use of a post-processing algorithm for the pre-processed PCd models.

The post-processing involves three primary steps: layering, sorting, and feature recognition. Scanned members inherently possess inner and outer surface layers, as depicted in Figure 4. However, the inner layer of a CFS member is challenging to scan comprehensively due to shaded reflections from the laser scanners. The thin-walled nature of CFS members allows the assumption that the inner and outer layers resemble each other. Consequently, the incomplete inner layer of the PCd models can be removed, leaving only the outer layer points. This process is carried out using Geomagic Wrap 2021 software [15].

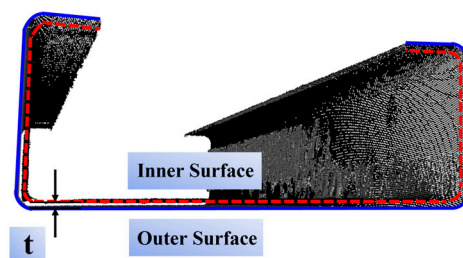


Figure 4. Inner and outer layers of the PCd.

The remaining PCd outer layer from the previous step needs to be organized since the point order from scanning is not conducive for structural analysis tasks like identifying dimensions and characterizing imperfections. The sorting process mirrors the method described by Zhao et al. [11]. Following the sorting, feature recognition is applied to the ordered section members. Typically, the cross sections of a CFS member comprise components such as a web, flanges, lips, and corners. Accurate dimensions, imperfection identification, and structural numerical simulations necessitate detailed geometric information of these member components. This need prompted the development of the feature recognition process, as detailed in the authors' previous work [8]. The measured cross sections undergo a sequential curvature test, wherein a formed circle progresses across the recognition region.

The segment exhibiting the maximum curvature is designated as the corner, while other segments are considered flat regions. Additionally, an optimization is conducted to ensure that the cross sections' features are recognized robustly and accurately (Figure 5).

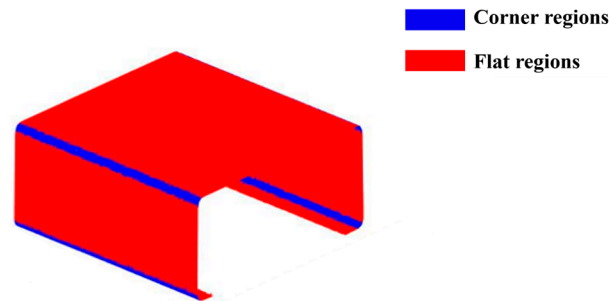


Figure 5. Cross Sections feature recognition.

2.3. Data Scheme

This research develops an accurate numerical simulation method for the as-true digital twins of CFS members, leveraging dense measurement point clouds. Twenty-seven CFS Cee members are examined experimentally to validate the numerical simulations and substantiate various modeling parameters. The nominal dimensions of the 27 CFS Cee members are presented in Table 1. The specimen's naming convention is illustrated in Figure 6.

Table 1. Measurement Scheme of CFS members.

Section ID	L (mm)	H (mm)	t (mm)	B (mm)	D (mm)	θ (°)
C1-H180-B70-t2.0-450	450	180	2.0	70	20	90
C2-H180-B70-t2.5-450	450	180	2.5	70	20	90
C3-H180-B70-t3.0-450	450	180	3.0	70	20	90
C4-H200-B70-t2.0-450	450	200	2.0	70	20	90
C5-H200-B70-t2.5-450	450	200	2.5	70	20	90
C6-H200-B70-t3.0-450	450	200	3.0	70	20	90
C7-H280-B70-t2.0-450	450	280	2.0	70	20	90
C8-H280-B70-t2.5-450	450	280	2.5	70	20	90
C9-H280-B70-t3.0-450	450	280	3.0	70	20	90
C10-H180-B70-t2.0-1200	1200	180	2.0	70	20	90
C11-H180-B70-t2.5-1200	1200	180	2.5	70	20	90
C12-H180-B70-t3.0-1200	1200	180	3.0	70	20	90
C13-H200-B70-t2.0-1200	1200	200	2.0	70	20	90
C14-H200-B70-t2.5-1200	1200	200	2.5	70	20	90
C15-H200-B70-t3.0-1200	1200	200	3.0	70	20	90
C16-H280-B70-t2.0-1200	1200	280	2.0	70	20	90
C17-H280-B70-t2.5-1200	1200	280	2.5	70	20	90
C18-H280-B70-t3.0-1200	1200	280	3.0	70	20	90
C19-H180-B70-t2.0-3000	3000	180	2.0	70	20	90
C20-H180-B70-t2.5-3000	3000	180	2.5	70	20	90
C21-H180-B70-t3.0-3000	3000	180	3.0	70	20	90
C22-H200-B70-t2.0-3000	3000	200	2.0	70	20	90
C23-H200-B70-t2.5-3000	3000	200	2.5	70	20	90
C24-H200-B70-t3.0-3000	3000	200	3.0	70	20	90
C25-H280-B70-t2.0-3000	3000	280	3.0	70	20	90
C26-H280-B70-t2.5-3000	3000	280	2.5	70	20	90
C27-H280-B70-t3.0-3000	3000	280	2.0	70	20	90

"D" lip length of a cross section. " θ " are the corner angles of the cross section.

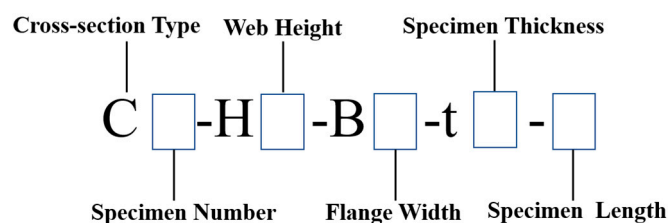


Figure 6. Specimen nomenclature.

3. A Simulation Method for Digital Twins of CFS Members

Digital twins accurately represent the real geometries of CFS members derived from post-processed laser measurements. However, the high density of these point clouds isn't always necessary, especially for numerical simulations considering CFS members' as-true geometry. The density of the point clouds should be reduced to a suitable amount to facilitate structural analysis via numerical simulation. This section introduces a simulation method using finite element modeling paired with digital twins of CFS members. The finite element analysis is executed using the ABAQUS CAE 2019 software, and appropriate modeling input files are generated accordingly.

3.1. Node Formation

Both material and geometric properties influence numerical simulations of structural members. While material properties can be ascertained through coupon testing, the geometric properties in simulations are derived from laser-based digital twins. However, the dense point clouds can't be used directly as nodes due to their high point density. Therefore, it's crucial to establish an appropriate mesh node configuration that reflects the accurate geometry while also de-sampling the measurement points for efficiency.

Given the assumption of a uniform cross-sectional thickness throughout a CFS member, the geometric characteristics of its central surface closely mirror that of its outer surface, as illustrated in Figure 4. Owing to the thin-walled nature of the member, points on the centerline section can be straightforwardly acquired by translating the outer surface points by half the thickness, represented as $\frac{t}{2}$.

The node formation begins with the line segments of a cross-section, such as the web, flanges, and lips. Considering the left-side flange as an example (Figure 7a), the flange is characterized through post-processing where the boundary points Q_1, Q_n are identified. The points Q_1 and Q_2 are linearly connected, setting the direction of this line as a local axis, represented by ζ . The lower point Q_1 , is designated as the origin. The perpendicular direction to the axis ζ is set as another principal axis η . Since the mesh size of the FE model is predetermined, the number of nodes on the cross-section and the distance between them can be ascertained. For instance, the left-side flange would have n nodes, as shown in Figure 7a. A linear interpolation is carried out with boundary points (Q_1, Q_2) . As a result, a series of points $\{q_1, q_2, q_3 \dots q_n\}$ with uniform distances are obtained.

The node formation continues with its foundation on the measurement point clouds. Since the points are sorted and organized in sequence, adjacent points line up in a cross-sectional array. For each interpolated point q_i , there are w measurement points in its vicinity. These points are linearly fitted, and then short line segments are obtained. The intersection between a fitted line segment and the axis η is considered a node Q_i . This procedure is repeated for the remaining mesh nodes of the flange till n equal-interval nodes are found. The final phase involves the formulation of mesh nodes for the centerline model. The normal direction of the flange, which coincides with the direction of the axis η , is identified. The translation displacement is half of the thickness $t/2$. Thus, the nodes are all shifted by $t/2$ along the direction η and the mesh nodes are obtained.

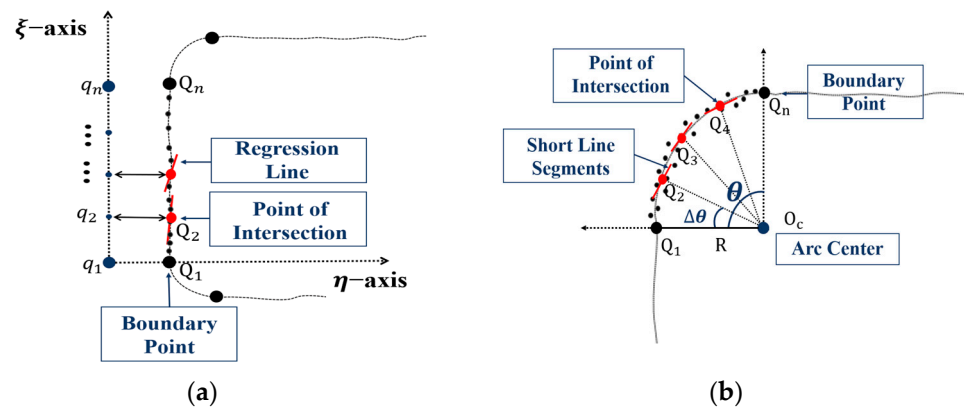


Figure 7. Point cloud data processing: (a) Left-side flange point cloud; (b) Corner point cloud.

The above line-segment nodes formation method applies to all linear regions of the cross sections. However, the corners of these cross-sections require a slightly modified approach due to their distinct geometry. Take the corner between a flange and a web, for example. The boundary points of this corner, denoted by Q_1 , Q_n , are obtained through the previously described post-processing algorithm. It is assumed that the corner can be fitted with an arc with radius R , the center of (O_c), which is set as the origin of the local polar coordinate. Similar to the line-segment formation, the number n and the angles $\Delta\theta$ interval of nodes of the corner are determined in advance, as shown in Figure 7b. The angle theta can be ascertained using Equation (1).

$$\Delta\theta = \frac{\theta}{n} \quad (1)$$

where θ is the angle of the corner obtained using the dimension-finding method applied to the measurement [deg.].

A series of interpolated points can be obtained using Equations (2) and (3):

$$q_i^p = R \times i\Delta\theta, \quad (2)$$

$$q_i = q_i^p + O_c, \quad (3)$$

where q_i^p represents the found point in the local coordinate; q_i are the coordinates of the interpolated points in the cross-section coordinate system.

The second step is the same as the process for line segments. Measurement points within a density distance d_i around q_i , determined by Equation (4), are utilized to fit a short line segment. The intersection between this short line segment and the fitted arc is treated as the desired node, translated by half of the thickness $\frac{t}{2}$ in the direction pointed to the origin O_c . Upon completion of this process, the node formation for corner segments is finalized. This methodology applies to all corner regions of standard CFS cross-sections.

$$d_i = \frac{|\tan(i\Delta\theta)x_i - y_i|}{\sqrt{1 + [\tan(i\Delta\theta)]^2}} \quad (4)$$

where (x_i, y_i) represents the point cloud node coordinates; d_i is the distance between point cloud coordinates and short lines [mm].

3.2. Finite Element Modeling

A script file for the ABAQUS software has been developed, a sample of which is attached in the Appendix. Key parameters related to the laser-measurement point clouds are listed in the section verified in the following sections.

3.2.1. Mesh Formation

The thickness of thin-walled members is comparatively minor relative to their other dimensions. Therefore, the simulation of CFS members, uses the S4R shell element for mesh. The mesh size typically necessitates an element with approximately equal length and width dimensions. The nodes along the member thus are established based on the total number of cross-section nodes, denoted as $N \times M$, where N is the number of cross-section nodes, and M is the number of longitudinal nodes. As illustrated in Figure 8, the nodes presented in the Script file comprise four columns, preceded by the '*NODE' keyword where "*" represents the beginning of the keyword in ABAQUS. The initial column indicates the numerical order, while the subsequent three columns delineate the coordinates relative to the x , y , z axes. Generally, the numerical order should be structured such that individual cross-sections are distinguishable. A recommended sequence is provided below in Equation (5):

$$\text{Number order} = (m - 1) \times 100 + n \tag{5}$$

where m is the m^{th} cross-section along the member, and n is the n^{th} node across the section.

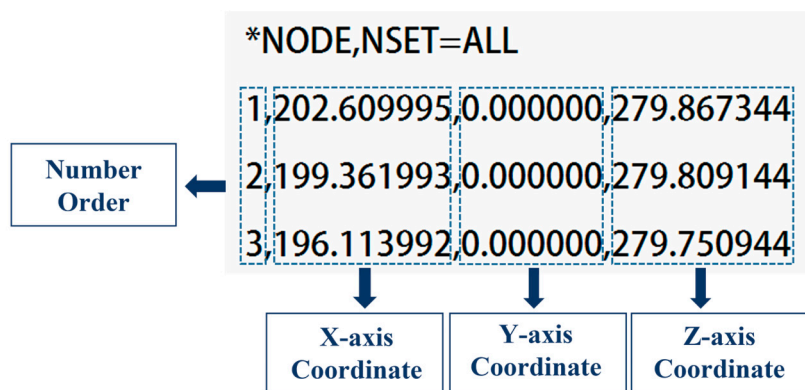


Figure 8. Node display of script file.

The node’s coordinates, especially the longitudinal coordinates, must be carefully treated. The original cross-section density is set at 1 mm. The value of M , representing the number of longitudinal nodes, should be calculated such that the result of L/M is an integer. Under this condition, the nodes of the cross-sections can be directly derived from the corresponding mesh nodes obtained from the previous step. Conversely, if L/M does not yield an integer, the nodes of the cross-sections can be obtained through interpolation from the neighboring nodes of the cross-sections.

Once the mesh nodes are determined, the mesh element can be formed using the S4R element type—a linear 4-node shell element with uniformly reduced integration. This is specified in the script file with the keyword '*Element, type S4R'. The data structure for this section is presented in five columns, as illustrated in Figure 9. The first column is the mesh element number order; a patch of typical mesh order numbers is illustrated in Figure 9. The subsequent four columns represent the number of orders of nodes. The second and third columns detail adjacent nodes, specifically the i^{th} and $i + 1^{th}$ nodes in the k^{th} cross-section, while the fourth and fifth columns describe the i^{th} and $i + 1^{th}$ nodes in a $(k + 1)^{th}$ cross-section.

3.2.2. Material Properties

In a finite element model, material properties typically encompass Young’s modulus (E), Poisson’s ratio (ν), the 0.2% yield strength ($\sigma_{0.2}$), the 0.5% yield strength ($\sigma_{0.5}$), and the ultimate strength (σ_{ult}). Additionally, for nonlinear analysis in finite element assessments, the stress-strain matrix is essential. These attributes are derived from material testing or existing experimental data in scholarly literature.

$(m-1) \times 100 + 1$	$(m-1) \times 100 + 2$	$(m-1) \times 100 + 3$	$(m-1) \times 100 + 4$	$(m-1) \times 100 + n - 1$	$(m-1) \times 100 + n$
$(n-1) \times (m-2) + 1$	$(n-1) \times (m-2) + 2$	$(n-1) \times (m-2) + 3$	$(n-1) \times (m-1)$	
$(m-2) \times 100 + 1$	$(m-2) \times 100 + 2$	$(m-2) \times 100 + 3$	$(m-2) \times 100 + 4$	$(m-2) \times 100 + n - 1$	$(m-2) \times 100 + n$
.....
$2 \times 100 + 1$	$2 \times 100 + 2$	$2 \times 100 + 3$	$2 \times 100 + 4$	$2 \times 100 + n - 1$	$2 \times 100 + n$
$n + 1$	$n + 2$	$n + 3$	$2n - 2$	
$100 + 1$	$100 + 2$	$100 + 3$	$100 + 4$	$100 + n - 1$	$100 + n$
1	2	3	$n - 1$	n

Figure 9. Order numbering of mesh element.

3.2.3. Boundary Condition

The boundary conditions in this research comprise the loading conditions and the restraint conditions. The boundary condition is assumed to be simply supported. A reference point at one end, RP1, is set to coincide with the centroid of the end cross-section. RP1 is rigidly tied to the end nodes, where it is permitted to have axial displacement and weak axis rotation. A reference point at the other end, RP2, is positioned at the centroid of the opposite end cross-section. Similarly, RP2 is rigidly tied to the end nodes, and this end is restricted to allow only weak-axis rotation.

Furthermore, the loading condition is displacement-controlled, a common approach in nonlinear structural analysis. The displacement is applied at RP1, permitting axial deformation. The initial displacement is set at $\frac{1}{100}$ of the member's length.

3.2.4. Analysis Step

The analysis step is essential in finite element modeling. Both the robustness and accuracy of the analysis are influenced by this step. Three main types of analyses are employed in thin-walled structural analysis: '*Static, general', '*Static, Riks', and '*Static, Stabilize'. The application of these steps is slightly different. The measurement contains a number of surface imperfections that result in divergence of '*Static, Riks' analysis method. The general method of '*Static, Riks', is unsuitable for large high-precision models based on laser measurement. The analysis step adopts '*Static, Stabilize'. A more comprehensive discussion of the analysis step can be found later in Section 6.2.2.

The energy consumption fraction is specified as 0.0002. This introduces an added viscous force to all nodes within the model. The magnitude of this force is dictated by the node's bit removal during time increments, stabilizing the model's computation. Additionally, parameters are set for the incremental steps: the maximum is 300, the initial is 0.001, the minimum increment is 1×10^{-5} , and the maximum increment is 0.05. These step parameters can be auto-generated for comparative analyses when executing the respective script files, ultimately determining the optimal input values.

4. Validation Testing

The paper proposes a method of numerical simulation methodology leveraging laser-measured digital twins. To ensure accurate replication of real CFS members' structural behavior, the finite element models must incorporate authentic geometry and precise material attributes. To validate this approach, axial compression tests are conducted on 27 distinct types of Cee members.

4.1. Material Testing

Material testing is conducted to obtain the material properties. While the CFS members are of the same steel grade, they vary in three different thicknesses. Consequently, three types of steel tensile coupons derived from the Cee members of differing thicknesses are examined. These steel tensile coupons are tabulated in Table 2 and visually depicted in Figure 10. All material testing procedures adhere rigorously to the Test Standard GB/T282.1-2021 [25,26]. The tests are performed using a 1000 kN microcomputer-controlled electro-hydraulic servo universal testing machine with a loading rate of 15 MPa/s, as shown in Figure 11.

Table 2. Design specifications for steel tensile coupons.

Name of Steel Tensile Coupons	Thickness (mm)	L_0 (mm)	L_c (mm)	L_t (mm)	S_0 (mm)	Number
Test1-2.0	2.0	90	130	250	40	3
Test2-2.5	2.5	95	135	255	50	3
Test3-3.0	3.0	100	140	260	60	3

L_0 is the original gauge length of testing specimens. L_c is the parallel length of testing specimens. L_t is the total length of the testing specimens. S_0 is the cross-section area of parallel regions.

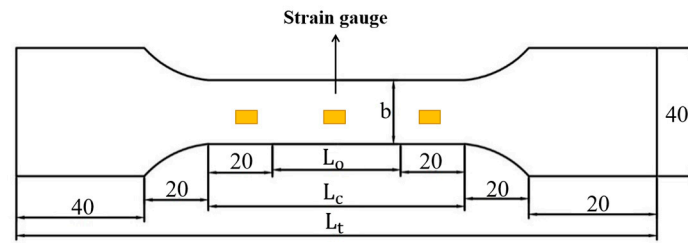


Figure 10. Steel tensile coupons (length unit: mm).



Figure 11. 1000 kN universal testing machine.

The results derived from testing necessitate processing for numerical simulation. The engineering stress-strain data are transformed into true data using Equations (6) and (7). The true material properties, ascertained from the tensile coupon tests, are detailed in Table 3. Poisson's ratio is designated as 0.3, a value commonly adopted for steel [7].

$$\sigma_{true} = \sigma_{eng}(1 + \varepsilon_{eng}), \quad (6)$$

$$\varepsilon_{true} = \ln(1 + \varepsilon_{eng}), \quad (7)$$

where σ_{true} and ε_{true} are the true stress and strain, respectively; σ_{eng} and ε_{eng} are the engineering stress and strain respectively.

Table 3. Material properties.

Name of Steel Tensile Coupons	Young's Modulus (MPa)	$\sigma_{0.2}$ (MPa)	$\sigma_{0.5}$ (MPa)	σ_{ult} (MPa)
Test1-2.0	196,000	455	489	556
Test2-2.5	196,000	440	477	551
Test3-3.0	196,000	392	431	506

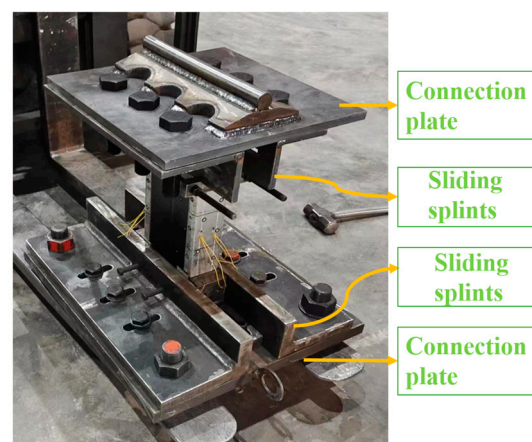
4.2. Design of the Validation Testing

4.2.1. Testing Set Up

In the validation testing, an axial compression experiment is conducted on simply supported Cee-shaped steel members. These specimens are positioned on a 50-ton loading apparatus comprising a reaction frame, a base, and a 50-ton actuator, as illustrated in Figure 12a. Simulating the boundary conditions is paramount to the success of the validation testing. For this purpose, a specific restraint device is designed, as shown in Figure 12a,b. This device is made up of three primary components: the articulated section ①, the connection plate ②, and the sliding splints ③. The articulated section is attached to either the actuator's loading cell or the base. The upper connection plate is designed with a hook, ensuring that the restraint's weight doesn't influence the specimens under test.



(a)



(b)

Figure 12. Experimental setup: (a) Simply supported restraint device. (b) Restraint device.

Additionally, the connection plates serve as intermediaries linking the articulated sections and the sliding splints. The articulated sections are welded onto the plates. These plates, in turn, support bolted splints equipped with sliding holes, facilitating adjustments to the loading applied to the specimens. Angle steels play a dual role, assisting in positioning the load and securing the specimens.

4.2.2. Sensor Arrangements

During the testing, two primary types of sensors are utilized: displacement sensors and strain gauges. As depicted in Figure 13a, seven displacement sensors are strategically positioned. Sensors W1 through W5 are dedicated to measuring horizontal deformations, whereas W6 and W7 capture vertical displacements. The average value from W6 and W7 provides the loading displacement of the specimen during the test.

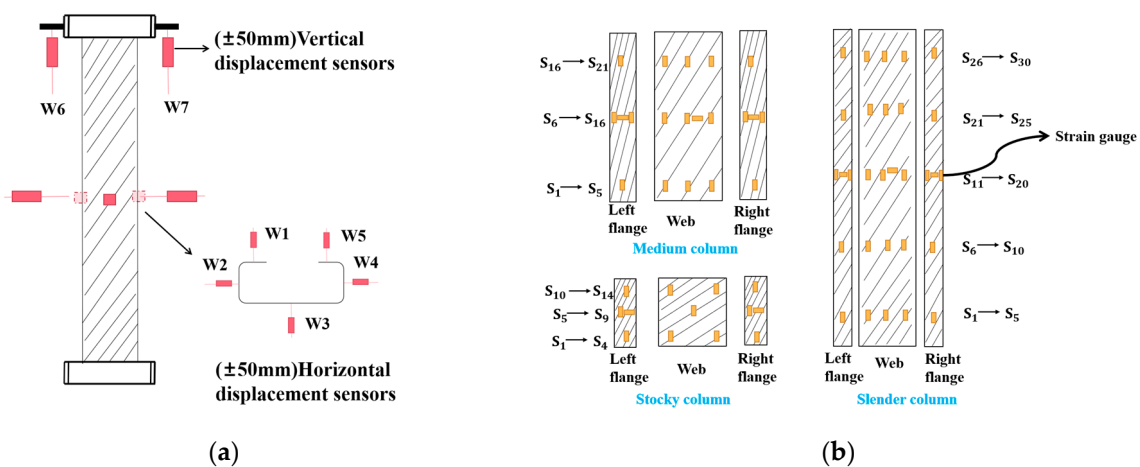


Figure 13. Sensor arrangements: (a) Displacement sensors; (b) Strain gauges.

Conversely, strain gauges are meticulously affixed around the specimens. The slender specimen is equipped with 30 strain gauges, the medium with 21, and the stocky specimen with 14. These gauges continuously record strain variations throughout the testing process. The arrangement of strain gauge locations for specimens of different lengths can be seen in Figure 13b.

4.3. Experimental Procedures

The testing is conducted rigorously in accordance with the ASCE Standard [4]. Before the primary loading, pre-loading is undertaken, where the maximum load does not exceed 5% of the calculated yield load. Initially, the loading procedure employs a load control approach, with increments of 10 kN, continued until no further load increases are observed. Following this, displacement control is initiated for post-peak behaviors that display significant deflection. Increments of 0.5 mm characterize the displacement-controlled stages, and each step persists for 2 min. The test concludes once the post-peak load falls below 60%.

It is imperative to highlight that the reaction frame and actuator are meticulously controlled during testing. The installation process is directed by laser projection to ensure precise alignment between the boundary device and the specimens. Additional measures, such as plumb and leveling tests, are used for verification. The sensors are methodically installed in sequence and undergo rigorous calibration.

5. Testing Results and Validation of Numerical Simulations

5.1. Testing Results

Testing targets 27 specimens varying in length, section size, and thickness. The results depicted in this research are the failure modes and peak loads where specimens are categorized as stocky columns, medium columns, and slender columns.

5.1.1. Failure Modes

(a) Stocky columns

The stocky column series consists of 9 members with three distinct cross-sectional types, each measuring 450 mm long. Most of the failure modes are material yielding with local buckling. Given the relatively large slenderness ratios, some members exhibit a combination of local and distortional buckling. Failure typically initiates at the web plate before extending to the adjacent flanges. The post-testing deformation is presented in Figure 14. An intriguing observation is that thinner specimens predominantly exhibit local buckling accentuated by material yielding. In contrast, the thicker specimens primarily exhibit combined buckling modes: distortional and local buckling. Moreover, the deformation in these thicker specimens tends to concentrate closer to their mid-span.

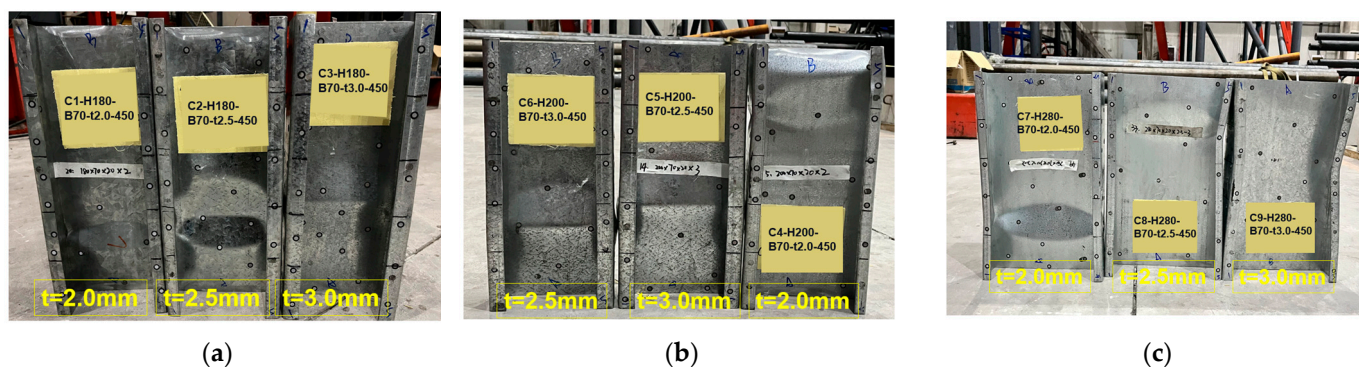


Figure 14. Deformation of stocky columns: (a) C-H180-B70; (b) C-H200-B70; (c) C-H280-B70.

(b) Medium columns

The medium column series comprises nine members, each showcasing one of three different cross-sectional types and three distinct thicknesses. Each column spans a length of 1200 mm. The exhibited failure modes comprise three buckling types: distortional, local, and global buckling about the weak axis, as illustrated in Figure 15. During the loading process, at approximately 60% of ultimate loads, distortion of the flanges becomes evident, predominantly in the middle to lower parts of the members. As loading intensifies, flange crippling is observed. Concurrently, global buckling of the member (manifesting as flexural bending) induces rotation in the articulated sections of the restraint devices, progressing until failure. Analogous to the observations in the stocky columns, the thicker the cross-section, the more the deformation tends to localize closer to the member's mid-span.

(c) Slender columns

The slender column series consists of nine specimens, each showcasing one of three different cross-sectional types and three distinct thicknesses, as depicted in Figure 16. These columns have a length of 3000 mm. The predominant failure mode for the slender columns is global buckling. When the applied load reaches about 50% of the ultimate load, distortional deformation begins to manifest, accompanied by a minor degree of flexural bending. Upon reaching the ultimate load, the articulated support undergoes rotation due to the pronounced global buckling.

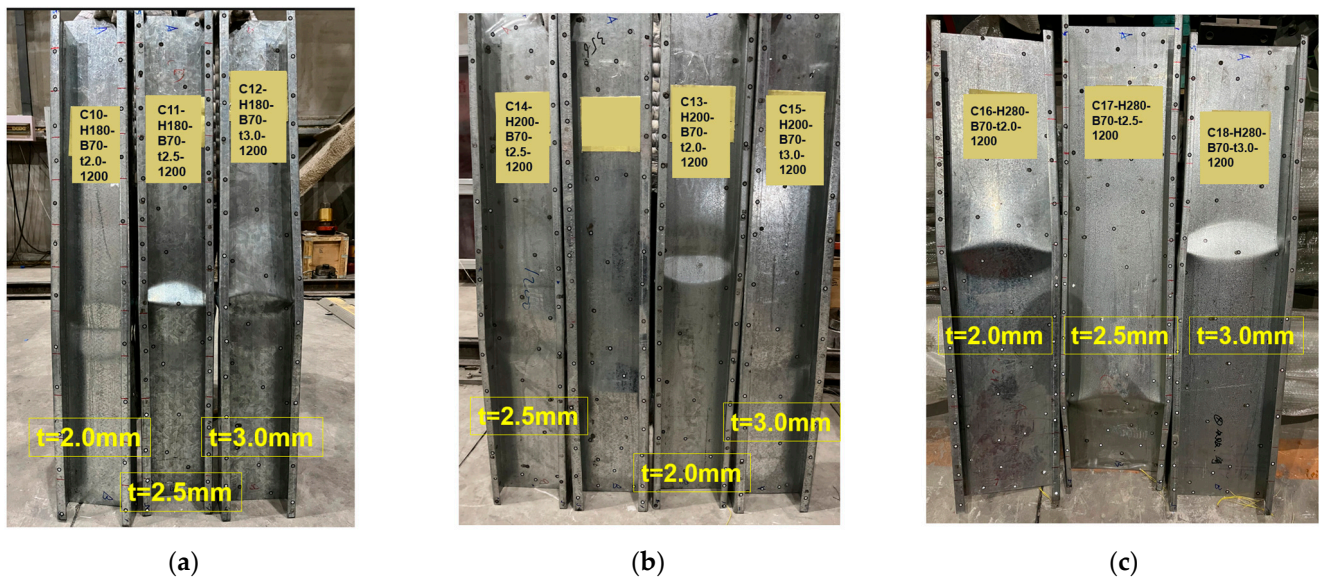


Figure 15. Deformation of medium columns: (a) C-H180-B70; (b) C-H200-B70; (c) C-H280-B70.

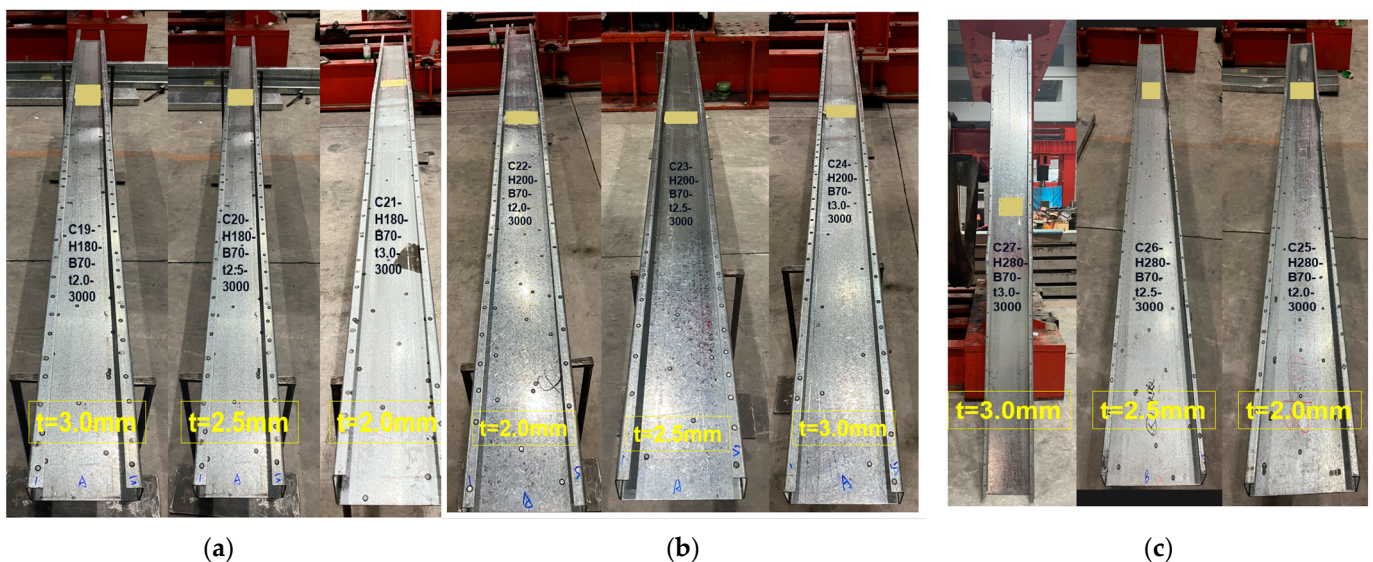


Figure 16. Deformation of slender columns: (a) C-H180-B70; (b) C-H200-B70; (c) C-H280-B70.

The differences in thickness are less pronounced when compared to the medium and stocky columns. The cross-section, specifically the slenderness ratio of the member, plays a more critical role in determining the failure modes. The C-H180-B70 manifests a combination of three distinct buckling modes: local, distortional, and flexural. In contrast, the cross-section C-H200-B70 predominantly displays evident web crippling, minor lip deformation, and subtle flexural bending. The cross-section C-H280-B70 exhibits pronounced distortional buckling, particularly at the lips and flanges, coupled with flexural bending.

5.1.2. Peak Loads

The peak load, representing the capacity of a member, is a pivotal metric for the design of structural members. CFS members, differing in cross-sections and thicknesses, were tested, with their peak loads summarized in Table 4. The average peak loads for stocky columns stand at 237.1 kN, while those for medium columns are 115.3 kN. The slender columns have an average peak load of 68.3 kN.

Table 4. Peak loads (P_{test}).

Stocky Columns	P_{test} (kN)	Medium Columns	P_{test} (kN)	Slender Columns	P_{test} (kN)
C1-H180-B70-t2.0-450	117.5	C10-H180-B70-t2.0-1200	71.6	C19-H180-B70-t2.0-3000	53.0
C2-H180-B70-t2.5-450	279.3	C11-H180-B70-t2.5-1200	73.89	C20-H180-B70-t2.5-3000	70.7
C3-H180-B70-t3.0-450	262.6	C12-H180-B70-t3.0-1200	152.9	C21-H180-B70-t3.0-3000	71.8
C4-H200-B70-t2.0-450	204.7	C13-H200-B70-t2.0-1200	102.6	C22-H200-B70-t2.0-3000	69.6
C5-H200-B70-t2.5-450	231.2	C14-H200-B70-t2.5-1200	108.2	C23-H200-B70-t2.5-3000	75.1
C6-H200-B70-t3.0-450	241.7	C15-H200-B70-t3.0-1200	149.7	C24-H200-B70-t3.0-3000	77.4
C7-H280-B70-t2.0-450	230.9	C16-H280-B70-t2.0-1200	116.0	C25-H280-B70-t2.0-3000	50.2
C8-H280-B70-t2.5-450	230.7	C17-H280-B70-t2.5-1200	116.5	C26-H280-B70-t2.5-3000	71.1
C9-H280-B70-t3.0-450	334.7	C18-H280-B70-t3.0-1200	146.5	C27-H280-B70-t3.0-3000	75.9

5.2. Validation of Finite Element Models

The numerical simulation method using the laser measurement is stated in Section 3. The section focuses on calibrating finite element models using results from validation testing. The calibration process primarily verifies the parameters outlined in Section 3.

5.2.1. Calibration of Parameters

- Boundary conditions:

Though various methods, such as laser line and leveler, were utilized to maximize the alignment accuracy of the longitudinal and transverse members during the testing, certain testing errors manifested due to the significant slender length of the medium-length column. In response to these errors, modifications were made during the simulation stage. Compared to the original centroid, the loading position of the slender column was shifted by 7–10 mm, and the medium column by 3–7 mm. No alterations were applied to the stocky column. This adjustment strategy was later corroborated through subsequent simulation and testing outcomes.

5.2.2. Peak Load Validation

The peak loads from DT-based numerical simulations are compared with testing results. These results are shown in Table 5. The deviation between these results is quantified through the calculation of difference ratios, as formulated in Equations (8) and (9):

$$\Delta_{DT} = P_{DT} - P_{test} \quad (8)$$

$$R_{DT} = \Delta_{DT} / P_{DT} \quad (9)$$

where Δ_{DT} is the load difference between the DT-based prediction and the testing result; R_{DT} is the ratio of the difference for the DT-based.

The differences between the finite element predictions and the experimental findings are reasonably modest. The most substantial deviation observed is approximately 10%. However, most discrepancies fall below the 5% threshold, a margin typically deemed acceptable in standard modeling analyses. Stocky columns exhibit the narrowest variations, owing to the ease of control during testing relative to their slender counterparts. Consequently, the outcomes of the numerical simulations are considered satisfactory.

5.2.3. Failure Modes Validation

Upon comparing the failure mode of the stocky column in numerical simulation (Figure 17), it is apparent that the failure is primarily dominated by distortional buckling and local buckling, with deformation concentrated at the mid-span. At this point, the materials transition into the plastic stage. Conversely, the simulated deformation of the medium column reveals a combination of deformation modes. Flexural buckling about the weak axis is evident, along with distortional and local buckling occurring at the mid-span and 1/3 height of the member, respectively. The slender column is primarily characterized by flexural buckling, with minor distortional buckling observable at the mid-span. Notably, the extent of local buckling in both the stocky and medium columns in the

numerical simulation is marginally less pronounced than that observed in the testing. This discrepancy merits careful consideration in the refinement and optimization of subsequent simulation methodologies.

Table 5. Comparisons of peak loads across different simulations.

Section ID	$P_{test}/(kN)$	$P_{DT}/(kN)$	$P_{trad}/(kN)$	$\Delta_{DT}/(kN)$	$R_{DT}/(\%)$	$\Delta_{trad}/(kN)$	$R_{trad}/(\%)$
C1-H180-B70-t2.0-450	117.6	129.3	124.1	11.7	9.1%	6.6	5.3%
C2-H180-B70-t2.5-450	279.3	301.2	277.6	21.8	7.3%	−1.8	−0.6%
C3-H180-B70-t3.0-450	262.6	261.2	315.6	−1.4	−0.5%	52.9	16.8%
C4-H200-B70-t2.0-450	204.7	207.2	156.0	2.5	1.2%	−48.6	−31.2%
C5-H200-B70-t2.5-450	231.2	225.9	292.4	−5.3	−2.3%	61.2	20.9%
C6-H200-B70-t3.0-450	241.8	237.4	260.6	−4.43	−1.9%	18.8	7.2%
C7-H280-B70-t2.0-450	230.9	210.0	247.9	−20.9	−9.9%	17.0	6.9%
C8-H280-B70-t2.5-450	230.8	246.8	204.1	16.0	6.5%	−26.7	−13.1%
C9-H280-B70-t3.0-450	334.7	304.9	375.2	−29.9	−9.8%	40.5	10.8%
C10-H180-B70-t2.0-1200	71.6	68.8	87.6	−2.8	−4.0%	16.0	18.3%
C11-H180-B70-t2.5-1200	73.9	71.6	97.9	−2.3	−3.3%	24.0	24.5%
C12-H180-B70-t3.0-1200	152.9	158.7	191.1	5.8	3.7%	38.2	20.0%
C13-H200-B70-t2.0-1200	102.6	105.1	124.4	2.4	2.3%	21.8	17.5%
C14-H200-B70-t2.5-1200	108.2	105.3	129.8	−3.0	−2.8%	21.6	16.6%
C15-H200-B70-t3.0-1200	149.8	144.0	182.1	−5.8	−4.0%	32.4	17.8%
C16-H280-B70-t2.0-1200	116.0	113.1	145.6	−2.9	−2.6%	29.6	20.3%
C17-H280-B70-t2.5-1200	116.5	124.4	156.5	7.9	6.3%	40.0	25.6%
C18-H280-B70-t3.0-1200	146.5	141.5	169.5	−5.0	−3.5%	23.0	13.6%
C19-H180-B70-t2.0-3000	53.0	56.3	64.7	3.3	5.9%	11.7	18.1%
C20-H180-B70-t2.5-3000	70.7	73.8	87.8	3.1	4.3%	17.1	19.5%
C21-H180-B70-t3.0-3000	71.9	72.0	85.7	0.2	0.3%	13.8	16.1%
C22-H200-B70-t2.0-3000	69.6	75.3	89.9	5.7	7.6%	20.3	22.6%
C23-H200-B70-t2.5-3000	75.1	77.8	96.5	2.7	3.5%	21.4	22.2%
C24-H200-B70-t3.0-3000	77.4	76.5	92.9	−0.9	−1.1%	15.5	16.7%
C25-H280-B70-t2.0-3000	50.2	53.5	61.1	3.2	6.1%	10.9	17.9%
C26-H280-B70-t2.5-3000	71.1	73.5	81.5	2.4	3.3%	10.5	12.8%
C27-H280-B70-t3.0-3000	75.9	69.1	90.6	−6.80	−9.8%	14.8	16.3%

5.2.4. Strain-Peak Load Curves

In this section, the accuracy denoted with R_{str} , of the DT-based model is validated by comparing the strain values generated by the DT-based model and the testing result at the left flange, web, and right flange under peak loads (Equation (10)). To achieve this, three stocky columns, three medium columns, and three slender columns were randomly selected for comparison from the tests. Strain data during testing were captured using strain gauges, as depicted in Figure 15b. These gauges were specifically positioned at the most prominent flange locations and web buckling within the members. Correspondingly, DT-based models for these nine members were chosen, ensuring that the locations for strain assessment mirrored those in the experimental setup.

$$R_{str} = |\varepsilon_{DT} - \varepsilon_{test}| / \varepsilon_{DT} \quad (10)$$

where ε_{DT} represent the strain derived from the DT-based prediction at peak load; ε_{DT} denote the strain from the test results at peak load; and R_{str} is the ratio of the difference between the DT-based prediction and the testing result.

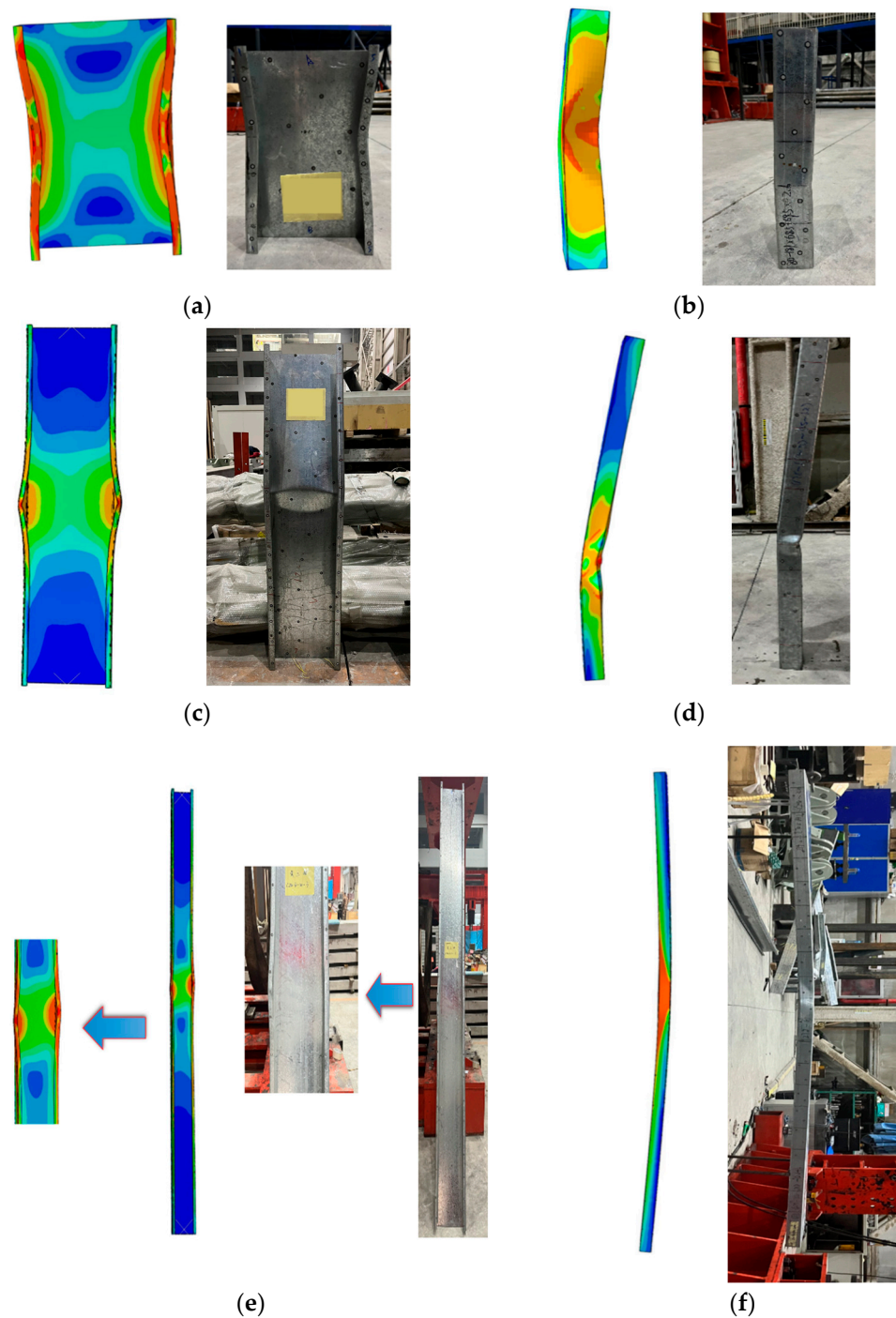


Figure 17. Failure modes validation for DT-based numerical simulation method: (a) Front view of stocky columns; (b) Side view of stocky columns; (c) Front view of medium columns; (d) Side view of medium columns; (e) Front view of slender columns; (f) Side view of slender columns.

To illustrate the predictive capabilities of the DT-based model more comprehensively, this study presents a comparative load-strain curve for a randomly selected member (C5-H200-B70-t2.5-450). The chosen points for analysis are S3, S6, and S8 (as shown in Figure 13b). In the initial loading phase, both the experimental results and the DT-based model indicated a consistent compressive state, suggesting an absence of localized buckling in the flange and web for both scenarios. As the applied load on the member intensified, reaching the buckling threshold, the experimental data and the DT-based model began to display signs of alternating concave-convex buckling patterns spanning multiple half-

wavelengths. At this point, the strain at the buckling location underwent a swift transition. The curve at this point denotes the member's critical buckling load value, characterized by the emergence of inflection points and pronounced member deformation. Additionally, it's essential to highlight that the initial alignment between the experimental results and the DT-based model is commendable. However, disparities emerge in the later stages. This divergence arises because the deformation direction becomes unpredictable when the model undergoes buckling, resulting in strain gauges experiencing compression and tension. In the DT-based model's context, the web area is uniformly compressed initially (as shown in Figure 18a). But as buckling sets in, it transitions to a state of tension, mirroring the phenomena observed in the experimental tests. Additionally, the strain values of the web at the end of the loading are also nearly identical. The strain values in the flange area of the stocky column during the testing and in the DT-based model align closely at the peak load (Figure 18b,c). However, discrepancies arise towards the end of the loading. This primarily stems from the fact that, post reaching the peak load in the testing, the strain gauges in this region undergo buckling, transitioning from compression to tension. In contrast, the strain gauges in the DT-based model consistently remain compressed.

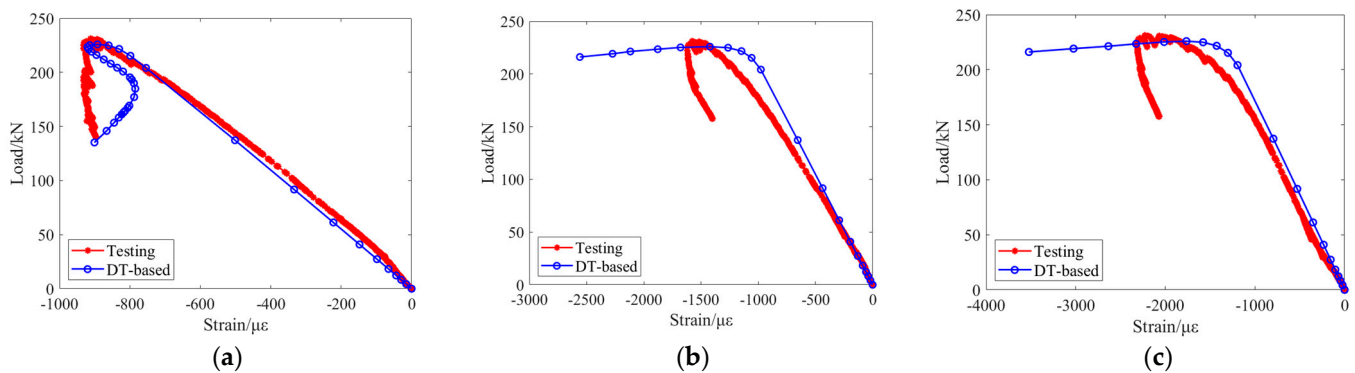


Figure 18. Load-strain curves of a typical column C5-H200-B70-t2.5-450: (a) Web (S6); (b) Left flange (S3); (c) Right flange (S8).

Considering the number of 27 members, not all load-strain curves could be displayed. Therefore, stocky, medium, and slender columns were chosen to compare their strains at peak load (Table 6). The average testing strain at the web position of the stocky column was $-1286.4 \mu\epsilon$, whereas the predicted strain by the DT-based model at this position was $-1288.5 \mu\epsilon$. The average percentage error (R_{str}) between the testing and predicted values for each stocky column at this location was 4.9%. The average testing strain at the web position of the stocky column was $-1679.9 \mu\epsilon$, while the DT-based model predicted $-1599.95 \mu\epsilon$, resulting in an error percentage of approximately 20.9%. Besides the stocky column, the testing and DT-based model strains at the web position of the medium column were $-291.4 \mu\epsilon$ and $-266.0 \mu\epsilon$, respectively, with a percentage error of 10.6%. The testing and predicted strains at the flange position of the medium column were $-1373.7 \mu\epsilon$ and $-1340.0 \mu\epsilon$, resulting in a percentage error of 15.5%. Lastly, the testing and DT-based model strains at the web position of the slender column were $196.0 \mu\epsilon$ and $223.5 \mu\epsilon$, respectively, with a percentage error of 12.0%. The testing and predicted strains at the flange position of the slender column were $-644.6 \mu\epsilon$ and $-739.2 \mu\epsilon$, resulting in a percentage error of 19.0%. It is worth noting that, overall, the predicted results for the web position are better than those for the flange position. This is because there is a certain error between the position of the strain gauges and the actual ideal state of the DT model, which results in more significant errors in strain measurements at the flange during loading.

Table 6. Comparisons of strains in columns at peak loads.

Section ID	DT-Based ($\mu\epsilon$)			Testing Results ($\mu\epsilon$)			$R_{str}(\%)$		
	Left Flange	Web	Right Flange	Left Flange	Web	Right Flange	Left Flange	Web	Right Flange
C2-H180-B70-t2.5-450	-2119.3	-1599.1	-1270.2	-1493.8	-1684.0	-1464.0	29.5	5.3	15.3
C5-H200-B70-t2.5-450	-1422.2	-892.1	-1764.3	-1578.9	-912.4	-2227.0	11.0	2.3	26.2
C7-H280-B70-t2.0-450	-1328.8	-1368.1	-1694.9	-1134.0	-1269.2	-2181.7	14.7	7.2	28.7
C14-H200-B70-t2.5-1200	-1732.3	-270.0	-917.7	-1729.1	-273.0	-652.3	0.2	1.1	28.9
C15-H200-B70-t3.0-1200	-1774.6	-207.6	-590.4	-1692.1	-254.1	-494.8	4.7	22.4	16.2
C17-H280-B70-t2.5-1200	-1499.0	-320.3	-1525.1	-1919.3	-347.0	-1754.6	28.0	8.3	15.1
C20-H180-B70-t2.5-3000	-814.4	292.9	-444.3	-799.5	228.6	-369.3	1.8	21.9	16.9
C22-H200-B70-t2.0-3000	-884.8	165.9	-676.8	-984.1	144.7	-452.8	11.2	12.8	33.1
C27-H280-B70-t3.0-3000	-1095.1	211.8	-519.6	-924.0	214.7	-337.6	15.6	1.4	35.1

Through statistical analysis and comparisons of the strain data at maximum loads between the DT-based models and testing results, it's evident that the DT-based model can effectively predict the strains of members under peak load. The numerical simulation approach, specifically the DT-based modeling, proves robust and accurate.

6. Discussion

6.1. Comparisons with Traditionally Numerical Simulations

The test outcomes are compared with traditional numerical simulations, wherein the initial buckling mode of a member serves as the imperfection shape, adopting a magnitude of $L/960$ as specified by standards [4,5]. A typical cross-section is selected for comparisons across different lengths. The shell element type is consistent with the laser measurement models, specifically S4R. The mesh sizes are kept uniform to facilitate better comparisons. Boundary conditions are set as simply supported, and the analysis step mirrors that of the measurement models. The outcomes of the finite element simulation, particularly the failure modes and peak loads, are meticulously compared.

6.1.1. Peak Load

The peak loads from traditional numerical simulations are compared with test results, as illustrated in Table 5. Difference ratios are derived from Equations (11) and (12):

$$\Delta_{trad} = P_{trad} - P_{test} \quad (11)$$

$$R_{trad} = \Delta_{trad} / P_{trad} \quad (12)$$

where Δ_{trad} is the load difference between predictions from traditional numerical simulations and the actual testing result.

R_{trad} is the ratio of the difference for the traditional numerical simulations.

The traditional numerical simulations method uses identical boundary conditions and loading modes as the DT-based method. However, when comparing the ultimate loads between the traditional and DT-based methods, the traditional approach underperforms relative to testing results. The average R_{trad} for the slender columns stands at 18.0%, while it is 19.3% for medium columns. These results indicate its inadequacy in accurately predicting the member's ultimate load. For stocky columns, the efficacy is slightly better at 12.5%. Conversely, the average R_{DT} for the DT-based numerical simulation method is 4.7% for slender columns, 3.6% for medium columns, and 5.3% for stocky columns. Moreover, the maximum R_{DT} does not exceed 10% for any specimen. The predictive accuracy of the traditional numerical simulations is significantly surpassed by the DT-based numerical simulation method.

6.1.2. Failure Modes

Compared with the testing failure modes, traditional numerical simulations display considerable discrepancies in deformation, as highlighted in Figure 19. Taking the stocky

column, C-H280-B70, as an example, there are evident differences in the failure positions, magnitudes, and modes. The medium column's behavior is similar to the stocky column, though the failure position is more proximal. Conversely, the slender column provides the closest simulation results to the testing, with matching failure mode types. However, the deformation's positioning is not consistent. A clear distinction between Figures 17 and 19 reveals that the traditional numerical simulation method is markedly less efficient than the DT-based method in these instances.

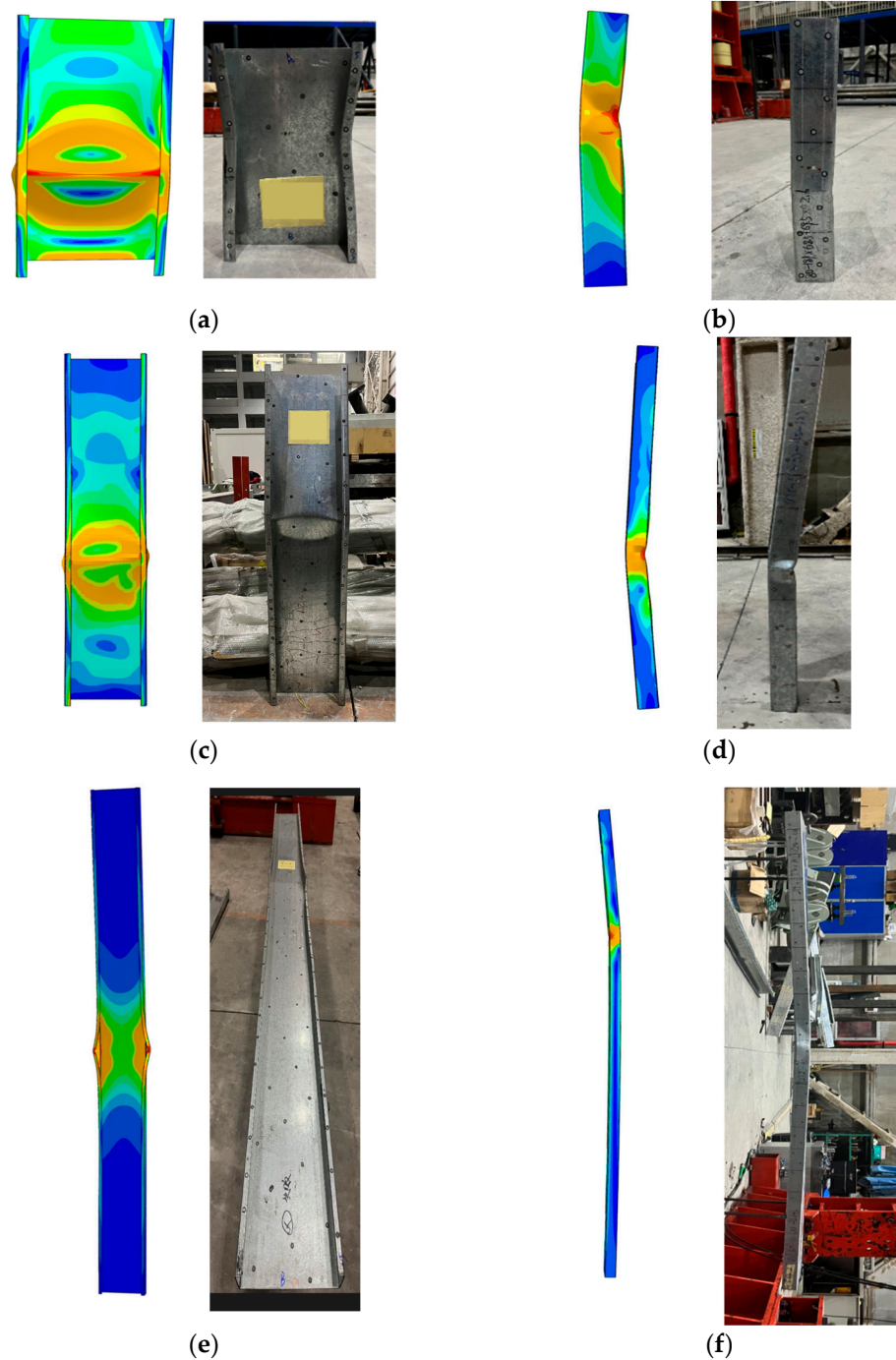


Figure 19. Failure modes validation for traditional numerical simulation method: (a) Front view of stocky columns; (b) Side view of stocky columns; (c) Front view of medium columns; (d) Side view of medium columns; (e) Front view of slender columns; (f) Side view of stocky columns.

6.2. Parametric Analysis

6.2.1. Mesh Density

Meshes sizes are evaluated for comparison when modeling the stocky, medium, and slender columns. The initial measurement density is overly congested, making it inefficient for numerical simulations. As a result, there's a need to de-sample the density of mesh nodes without compromising simulation accuracy. In contrast to the original cross sections, the de-sampled models display 1/5 and 1/10 of the mesh densities, as depicted in Figure 20. The findings presented in Figure 21 indicate that de-sampling the cross-section densities has a negligible impact on the numerical simulations, with the predicted ultimate load value differing by no more than 1 kN. Additionally, computation efficiency is significantly enhanced, ranging from 50% to 70%.

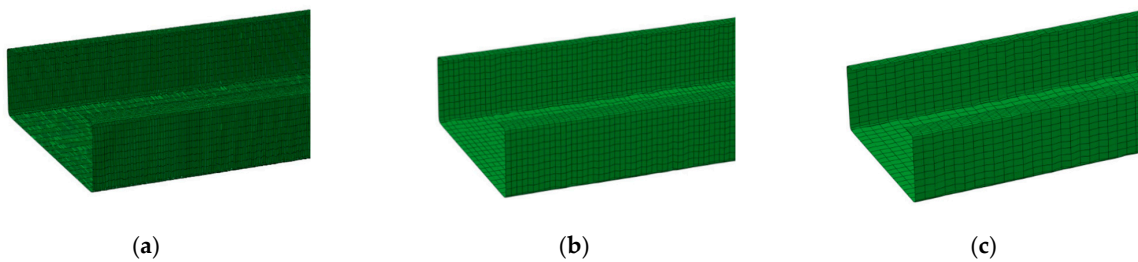
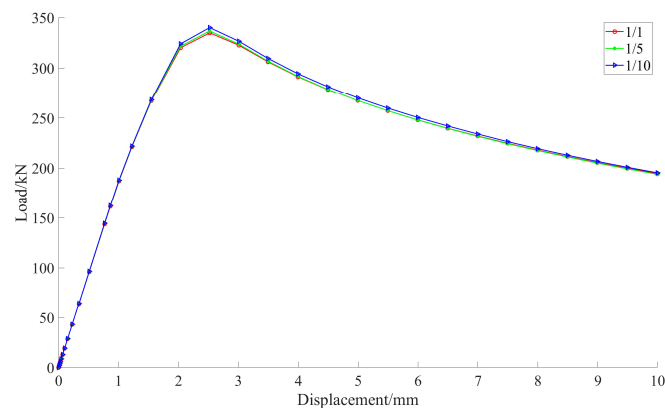
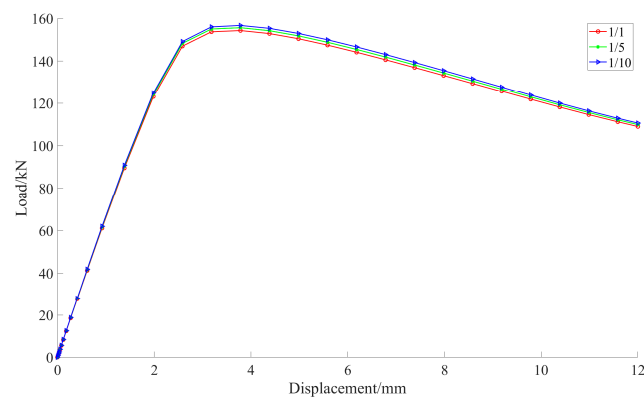


Figure 20. Mesh densities: (a) Normal mesh density; (b) One-fifth of the normal mesh density; (c) One-tenth of the normal mesh density.

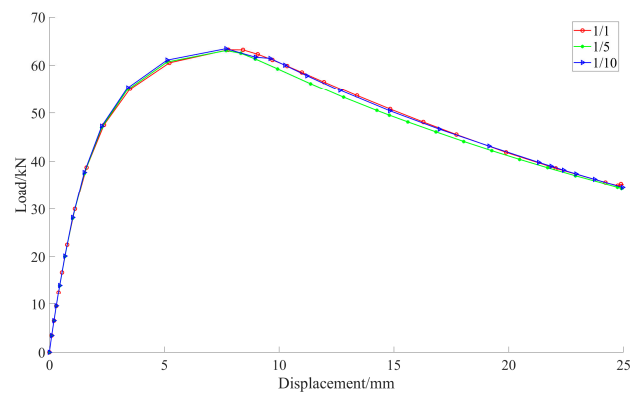


(a)



(b)

Figure 21. Cont.

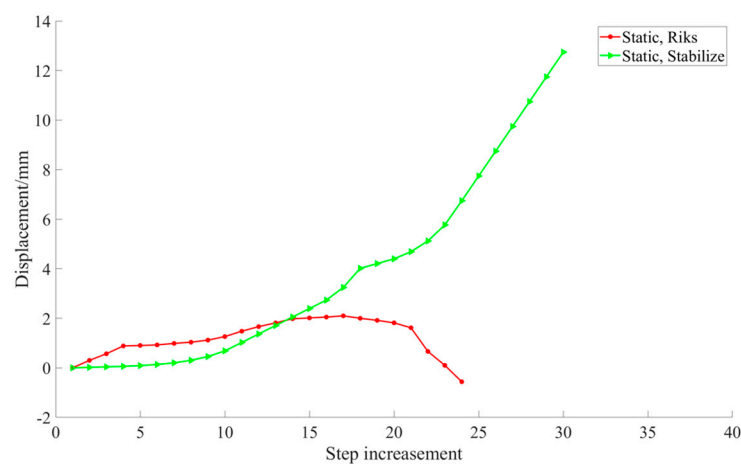


(c)

Figure 21. Load-displacement of different density mesh: (a) Stocky columns; (b) Medium columns; (c) Slender columns.

6.2.2. Analysis Step

The ‘Static, Riks’ method is frequently employed in traditional numerical simulation methods for CFS members during the analysis phase. However, a challenge emerges when working with extensive, high-precision numerical models grounded in real-world measurements. Whether analyzing stocky, medium, or slender columns, the ‘Static, Riks’ analysis step often struggles with convergence. This phenomenon is visualized in Figure 22, where the X-axis represents the number of analysis steps, and the Y-axis indicates the centroid displacement of the member’s compressed end. Given a scenario where the member undergoes compression, leading to a downward movement of the centroid, the Y value becomes positive. When employing the ‘Static, Riks’ method, the initial phase showcases that the member can be compressed due to axial force. Yet, with an increase in the number of analysis steps, the model’s iterative efficacy starts to wane. This is highlighted by the displacement turning negative, an outcome contrary to what’s observed in real-world testing.



(a)

Figure 22. Cont.

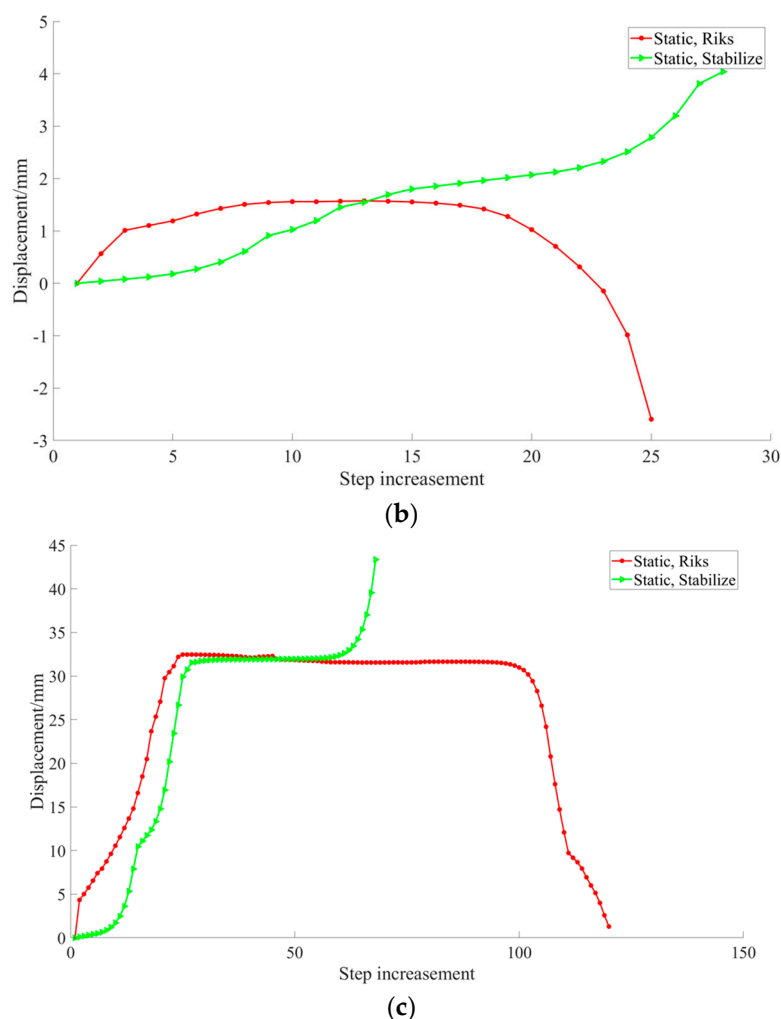


Figure 22. Step increase-Displacement of different step types: (a) Stocky columns; (b) Medium columns; (c) Slender columns.

On the other hand, utilizing the ‘Static, Stabilize’ method for the analysis steps, as depicted in Figure 21, ensures that the iterative performance of the model remains consistent even with an increase in analysis steps, avoiding the non-convergence issue altogether. Further, when comparing the simulated peak load of the DT model in Table 5 to the experimental peak load, coupled with the failure mode examination in Figure 17, it becomes evident that the DT simulation, when employing the ‘Static, Stabilize’ analysis step, provides a precise and resilient replication of experimental conditions. As a result, for this simulation, the ‘Static, Stabilize’ method was the preferred choice for the analysis step.

7. Conclusions

This paper systematically introduces a new DT-based numerical simulation method that utilizes the as-true geometries of CFS sections captured by a 3D laser scanner. This offers a fresh perspective on simulating the authentic defects observed in cold-formed steel members. The Digital Twin (DT)-based simulation method leverages these as-true geometries from the CFS sections. This method utilizes the reconstructed measurement point clouds in finite element modeling, ensuring the retention of true geometric features. To validate the modeling choices, including mesh sizes and boundary conditions, a comprehensive series of tests, encompassing material testing and axial compression testing, was conducted. The superiority of the DT-based numerical simulation method is highlighted through its comparison with the conventional numerical simulation. The latter typically only accounts for the first mode imperfection in CFS member geometry.

1. This paper introduces a newly developed DT-based numerical simulation method for Cee-section CFS members, which harnesses detailed geometries derived from laser scanning techniques. The dense measurement point clouds are de-sampled using heuristic guidelines to preserve essential geometric features. Finite element modeling is executed by scripting an ABAQUS running file using a suffix script. Key modeling parameters are identified and refined through empirical testing.
2. Axial compression tests were conducted on 27 Cee-shaped CFS members, varying in lengths, sections, and thicknesses. Results from these tests were juxtaposed with model analysis outcomes, revealing a commendable alignment between the observed phenomena and the DT-based numerical simulations. The average discrepancy between the tested and simulated ultimate loads stood at 5.3% for stocky columns, 3.6% for medium columns, and 4.7% for slender columns. Moreover, the strain values at peak loads from the DT-based model's critical points closely mirrored the test findings, with an average error of approximately 13.8% between the web and flange. Thus, the DT-based numerical simulation method effectively predicted the specimen's failure mode and peak load.
3. The DT-based numerical simulation method was benchmarked against the conventional numerical simulation approach for CFS member structural performance modeling. When juxtaposed with this traditional method, the DT-based simulation consistently outperformed in predicting structural behaviors, notably in areas like load capacities and failure modes.

The DT-based numerical simulation method demonstrates both efficiency and accuracy in predicting structural performance. This approach establishes a robust foundation for future research in intelligent structural analysis of CFS members. This method stands out when the goal is high efficiency and precise modeling predictions, especially for training surrogate models. Emerging system-based or simulation-based design approaches can also leverage the advantages of this simulation method.

Author Contributions: Conceptualization, X.Z.; methodology, P.D. and X.Z.; validation, X.S. and P.D.; data analysis, P.D. and X.Z.; experimental design, P.D., X.S. and X.Z.; data curation, P.D.; writing—original draft, P.D. and X.Z.; writing—review and editing, X.Z. and Z.Z.; visualization, P.D.; supervision, X.Z.; funding acquisition, X.Z. and G.D. All authors have read and agreed to the published version of the manuscript.

Funding: This research was funded by the Youth Program of the National Natural Science Foundation of China under grant number 52208141. A portion of this work received support from the Ministry of Housing and Urban-Rural Development Science and Technology Plan Project, with the grant number 2020-K-094. The students are also sponsored by the BUCEA Post Graduate Innovation Project, with the grant number PG2023034.

Data Availability Statement: The data used in this study will be made available upon request.

Acknowledgments: This research was primarily funded by the Youth Program of the National Natural Science Foundation of China, Grant No. 52208141. Additional support was provided by the Ministry of Housing and Urban-Rural Development Science and Technology Plan Project, Grant No. 2020-K-094, and the Beijing Energy Conservation & Sustainable Urban and Rural Development Provincial and Ministry Co-construction Collaboration Innovation Center. The students are also sponsored by the BUCEA Post Graduate Innovation Project, with the grant number PG2023034. The opinions, findings, conclusions, or recommendations presented in this material are solely those of the authors and do not necessarily reflect the views of the sponsors or other affiliated entities.

Conflicts of Interest: The authors declare no conflict of interest.

References

1. Lechner, B.; Pircher, M. Analysis of imperfection measurements of structural members. *Thin-Walled Struct.* **2005**, *43*, 351–374. [[CrossRef](#)]
2. Amouzegar, H.; Amirzadeh, B.; Zhao, X.; Schafer, B.; Tootkaboni, M. Statistical analysis of the impact of imperfection modes on collapse behavior of cold-formed steel members. In Proceedings of the Structural stability Research Council Annual Sta, Nashville, TN, USA, 24–27 March 2015.
3. Farzaniyan, S.; Louhghalam, A.; Schafer, B.; Tootkaboni, M. Geometric imperfection models for CFS structural members, Part I: Comparative review of current models. *Thin-Walled Struct.* **2019**. [[CrossRef](#)]
4. *AISI S240-15*; North American Standard for Cold Formed Steel Structural Framing. American Iron and Steel Institute: Washington, DC, USA, 2015.
5. *G. 50017-2017*; Steel Structure Design Standard. China Construction Industry Press Beijing: Beijing, China, 2017.
6. Zhao, X. Measurement and Application of Geometric Imperfections in Cold-Formed Steel Members. Ph.D. Thesis, Johns Hopkins University, Baltimore, MD, USA, 2016.
7. Ahmed, H.; Ghosh, S.; Mangal, M. Probabilistic estimation of the buckling strength of a CFS lipped-channel section with Type 1 imperfection. *Thin-Walled Struct.* **2017**, *119*, 447–456. [[CrossRef](#)]
8. Zhao, X.; Wang, G.; Sun, X.; Wang, X.; Schafer, B. Modeling of uncertain geometry of cold formed steel members based on laser measurements and machine learning. *Eng. Struct.* **2023**, *115578*, 279. [[CrossRef](#)]
9. Schafer, B.; Pekoz, T. Computational modeling of cold-formed steel: Characterizing geometric imperfections and residual stresses. *J. Constr. Steel Res.* **1998**, *47*, 193–210. [[CrossRef](#)]
10. Feng, P.; Zou, Y.; Hu, L.; Liu, T. Use of 3D laser scanning on evaluating reduction of initial geometric imperfection of steel column with pre-stressed CFRP. *Eng. Struct.* **2019**, *198*, 109527. [[CrossRef](#)]
11. Zhao, X.; Tootkaboni, M.; Schafer, B. Laser-based cross-section measurement of cold-formed steel members: Model reconstruction and application. *Thin-Walled Struct.* **2017**, *120*, 70–80. [[CrossRef](#)]
12. Sun, Z.; Zheng, Y.; Sun, Y.; Shao, X.; Wu, G. Deformation ability of precast concrete columns reinforced with steel-FRP composite bars (SFCBs) based on the DIC method. *J. Build. Eng.* **2023**, *68*, 106083. [[CrossRef](#)]
13. Mai, B.; Pham, C.; Hancock, G.; Nguyen, G. Block shear strength and behaviour of cold-reduced G450 steel bolted connections using DIC. *J. Constr. Steel Res.* **2019**, *157*, 151–160. [[CrossRef](#)]
14. Keyence. High-Speed 2D/3D Laser Scanner LJ-V7000 Specification. Available online: <http://www1.keyence.com/topics/measure/ljv/ljv7000/ljv7000.php?ad=gapress1212prljv> (accessed on 16 August 2023).
15. *Geomagic*, Version 2013.0.2 [Computer Software]; Geomagic, Inc. and 3Dsystems, Inc.: Hangzhou, China, 2013.
16. Xu, Y.; Zhang, M.; Yang, S.; Zheng, B. Measurement and qualification of welded I-column failure mode using laser scanning technique. In *Structures*; Elsevier: Amsterdam, The Netherlands, 2021; Volume 34, pp. 2694–2707.
17. Zhao, X.; Tootkaboni, M.; Schafer, B. Development of a laser-based geometric imperfection measurement platform with application to cold-formed steel construction. *Exp. Mech.* **2015**, *55*, 1779–1790. [[CrossRef](#)]
18. Grieves, M. Digital twin: Manufacturing excellence through virtual factory replication. *White Pap.* **2014**, *1*, 1–7.
19. Zhang, H.; Liu, Q.; Chen, X.; Zhang, D.; Leng, J. A digital twin-based approach for designing and multi-objective optimization of hollow glass production line. *IEEE Access* **2017**, *5*, 26901–26911. [[CrossRef](#)]
20. Zhang, Z.; Hui, P.; Gu, C.; Xu, P.; Wu, Y.; Hua, Z. Buckling of cold-stretched cylindrical vessels under external pressure: Experimental and numerical investigation. *Thin-Walled Struct.* **2018**, *131*, 475–486. [[CrossRef](#)]
21. Xu, Y.; Wu, B.; Zheng, B. Full-field geometric imperfection and effect on cross-section capacity of circular steel tubes. *J. Constr. Steel Res.* **2023**, *201*, 107749. [[CrossRef](#)]
22. Farzaniyan, S.; Louhghalam, A.; Schafer, B.; Tootkaboni, M. Geometric imperfections in CFS structural members: Part I: A review of the basics and some modeling strategies. *Thin-Walled Struct.* **2023**, *186*, 110619. [[CrossRef](#)]
23. Aktepe, R.; Erkal, B. Experimental and numerical study on flexural behaviour of cold-formed steel hat-shaped beams with geometrical imperfections. *J. Constr. Steel Res.* **2023**, *202*, 107774. [[CrossRef](#)]
24. Nie, B.; Xu, S.; Zhang, Z.; Li, A. Surface morphology characteristics and mechanical properties of corroded cold-formed steel channel sections. *J. Build. Eng.* **2021**, *42*, 102786. [[CrossRef](#)]
25. *GB/T 228.1-2021*; Metallic Materials-Tensile Testing-Part 1: Method of Test at Room Temperature. Standards Press of China: Beijing, China, 2021. (In Chinese)
26. Galambos, T.V. (Ed.) *Guide to Stability Design Criteria for Metal Structures*; John Wiley & Sons: Hoboken, NJ, USA, 1998.

Disclaimer/Publisher's Note: The statements, opinions and data contained in all publications are solely those of the individual author(s) and contributor(s) and not of MDPI and/or the editor(s). MDPI and/or the editor(s) disclaim responsibility for any injury to people or property resulting from any ideas, methods, instructions or products referred to in the content.